2024 IEEE/ASME International Conference on Advanced Intelligent Mechatronics (AIM)
July 15-19, 2024. Boston, MA, USA

ExoNav: A Novel Robotic Steering and Latching Mechanism for Spinal Cord Stimulation Electrodes

Harshith Jella, Behnam Moradkhani, Pejman Kheradmand, Ajmal Zemmar and Yash Chitalia

***Abstract*— Robotic steering mechanism can be useful in the placement of electrodes in spinal cord stimulation (SCS) procedures. This paper introduces an innovative steering and latching mechanism called the ExoNav, designed for spinal cord stimulation electrodes. By applying magnetic locking in the robotic system, a non-contact stabilization is established at the robot's base to reduce tendon-sheath coupling effects that are common in continuum robots. A kinematic model has been developed and validated to predict the robot's behavior when subjected to tendon actuation. To broaden the analysis, a comparative assessment is performed by comparing robot behavior in an experimental setup involving a free base, with one stabilized by an external magnet. Finally, proof-of-concept trials with a surgeon demonstrate the capability of the ExoNav robot in phantom spinal cord models.**

I. Introduction

Chronic pain is one of the most prevalent medical challenges that affects nearly 1 billion patients worldwide and an estimated 100 million people in the United States [1]. For approximately 30% of these patients, conservative medical measures do not provide successful pain relief and the patients become surgical candidates. For patients who are not candidates for traditional spine surgery (i.e. if pain is present but no surgical pathology can be identified or a pathology is identified but the patient is not a good surgical candidate) or for patients in whom traditional spine surgery fails (e.g. complex regional pain syndrome), spinal cord stimulation (SCS) is a surgical option [2]. Here, electrical current is delivered to the dorsal column pain pathway to interfere with the pain perception of the patient. With the increasing prevalence of pain, SCS has become increasingly relevant. Currently, an estimated 50,000 cases are performed worldwide and the field is projected to significantly increase in the next 5 years [3].

SCS implantation is divided in 2 steps: (i) a trial to determine whether the patient benefits from the stimulation and (ii) the permanent implantation upon successful trial. To maximize the benefit during the trial, the stimulator is usually implanted precisely in the spinal midline. Accurate device steering is currently guided by hand and can be challenging.

H. Jella, B. Moradkhani, P. Kheradmand, and Y. Chitalia are with the Healthcare Robotics and Telesurgery (HeaRT) Laboratory, Speed School of Engineering, University of Louisville, Louisville, KY, USA.

A. Zemmar is with the Department of Neurosurgery, Zhengzhou University People's Hospital, Zhengzhou, China.

A. Zemmar is with the Department of Neurological Surgery, University of Louisville School of Medicine, Louisville, KY, USA..

H. Jella and B. Moradkhani have contributed equally to this work. A. Zemmar and Y. Chitalia contributed equally to senior authorship.

Corresponding author: Harshith Jella (harshith.jella@louisville.edu)

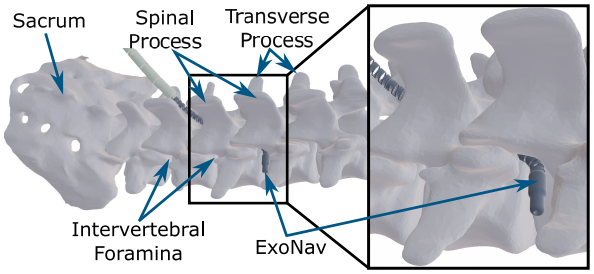

Fig. 1: ExoNav robotic system bending away from the midline within the spine.

During SCS lead placement, a passive guidewire with a beveled tip is inserted into the electrode body through a hollow lumen. The guidewire is manually navigated and steered by the physician at the tail of the electrode by translation and rotation to control the direction of its tip that is placed in the spinal epidural space. This method is challenging when the electrode must be navigated over longer paths to a target spinal segment, around obstacles or sharp curves. In about 20-40% of cases, physicians struggle to place the stimulator accurately, which can result in unsuccessful trials, significantly prolonged operative time and suboptimal benefit for the patient. With the current standard, the position of the SCS lead cannot be changed during the trial period to determine the ideal location for stimulation.

Thus far, very few studies have addressed these challenges. In [4], a method using a malleable disposable suture retrieval snare was presented to precisely position the epidural electrode in either a midline or paramedian position. The rigidity and dimensions of the snare used in this method make it unsuitable for precise lead position deviating from the midline or paramedian position. In another study [5], a magnetically guided catheter for SCS lead implantation was introduced, but lack of precise kinematic model and nonlinear behaviour of the magnetically actuated catheters makes it difficult to adopt this method for lead implantation.

In principle, the purpose of steering the SCS electrode is similar to using guidewires in endovascular procedures. Significant progress has been made in the design, manufacturing, and control of robotic guidewires. Steerable catheters/guidewires can be classified into four groups: tendon-driven [6]–[10], magnetically-navigated [11], [12], soft-material driven [13], or a combination of more than one of the above. Tendon-driven actuation is the most popular for guidewire design, but it has size constraints due to tendon routing [14]. For our application, the anatomical environment of the spinal epidural space permits enough space to have a bulkier structure that can encompass the lead externally. Another major limitation of tendon-driven actuation for long and flexible structures is tendon-sheath coupling. In other

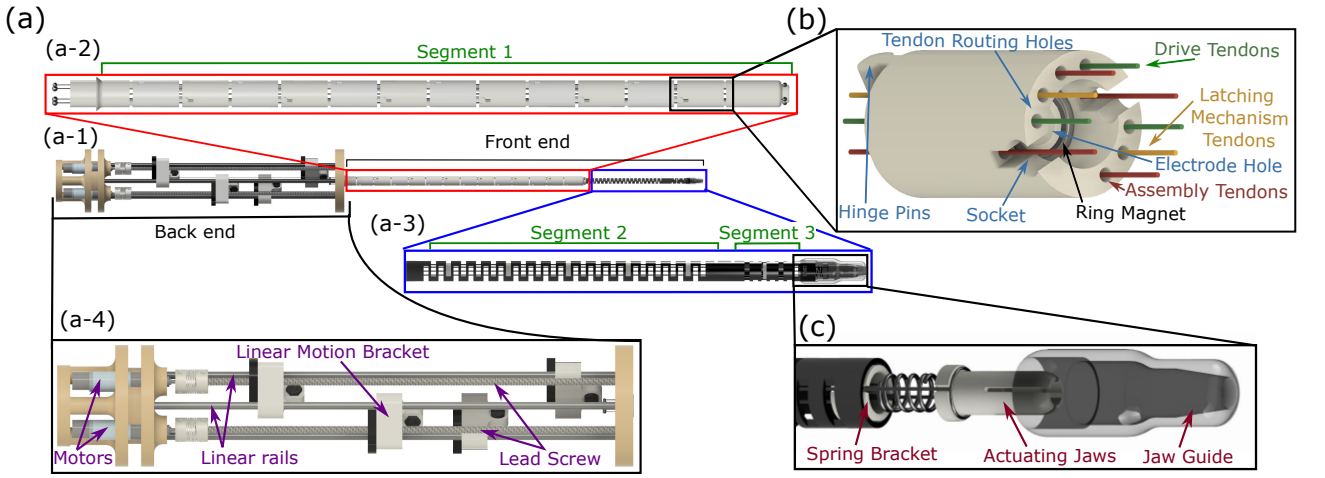

Fig. 2: (a) Overall design of the ExoNav displaying different segments (b) Individual link of the compound tube (c) Components of the latching mechanism

words, actuating a tendon fixed to the distal end of a robotic catheter results in unintended motion in the proximal sheath of the device. Some novel techniques have been proposed in recent times to minimize this coupling, using pneumatic cushion-like supports to stabilize tools [15]. However, in cases of epidural steering, where perforation of the dura, or core can pose a risk to the patient, contact-based stabilization cannot be applied.

In this work, we propose a novel robotic tool for SCS lead steering and implantation (shown in Fig. 1. The proposed robot is made of two different parts: the 3D-printed proximal compound tube, as seen in Fig. 2(a-2), and the distal asymmetrically notched two degree-of-freedom (2-DoF) nickel titanium (nitinol) tube, which is shown in Fig. 2(a-3). There are multiple magnets implemented inside the proximal tube which give us the ability to use an external magnetic field to achieve magnetic stabilization. This unique magnetic locking strategy helps to minimize the tendon-sheath coupling during distal tip steering. This type of stabilization is non-invasive, in that no physical contact with epidural anatomy is needed to achieve stabilization. The distal nitinol tube is actuated via tendons and can bend in different directions to reach to targets. We have also designed a unique latching mechanism at the tip of the robot, which can be used to latch to the SCS lead while the robot is steering and unlatch when the robot is at the desired target and ready to be retracted. The following are the major novel contributions of this work:

1) This is the first intrinsically actuated robotic solution to guide SCS electrode leads to target regions.
2) An entirely novel latching mechanism is proposed that acts as a gripper to hold and deliver SCS electrodes as the electrodes are navigated to a target site along the spinal cord.
3) While shape-locking stabilizing tools have been proposed in the past [15], this is the first work to propose a non-contact based stabilizing solution for continuum tendon-driven robots to minimize the aforementioned tendon-sheath coupling.

The remainder of the paper is organized as follows: Section II describes the front and back-end design of our robot, Section III presents the proposed mathematical model, Section IV describes and displays the results of the experiments. Finally, Section V concludes the paper with a comprehensive overview of the project and final remarks.

II. Robot Design

Fig. 2(a) shows the complete design of the robot. ExoNav comprises two primary components, as seen in Fig. 2(a-1): the front-end and the back-end. The front-end encompasses the continuum robot section of the design, while the back-end houses the actuation stage.

A. Front-end Design

The front-end design of the ExoNav is primarily comprised of two components: a 3D-printed compound tube (shown in Fig. 2(a-2)) with links consisting of embedded ring magnets for magnetic locking (depicted in Fig. 2(b)), and a distal 2-DoF machined nitinol tip (illustrated in Fig. 2(a-3)) which allows for distal steering.

1) 3D-Printed Compound Tube: As it is shown in 2(a-2), the 3D-printed compound tube consists of a simple interlocking design with alternating hinges in order to achieve two DoFs [16]. The tube has a diameter of 7 mm and each link contributes 14.88 mm to the length of the assembly. In the final assembly, twelve alternating links are used along with two modified links to interface with the back-end (consisting of the mechatronics to drive the robot) and the distal tip segment (made of 2-DoF nitinol joints). Fig. 2(b) shows the structure of a standard link consisting of pins and sockets to interface with each other. The link interfacing with the back-end contains only pins to begin the chain of links, while the link interfacing with the nitinol tube only has sockets and also reduces the circumference of the tendon routing to guide tendons into the nitinol tube. Each link was printed on a ProJet MJP 2500 and is comprised of two hinge pins, two perpendicular sockets, nine tendon routing channels around the circumference, and a central 2 mm hole through which the electrode travels.

The clearance of the tendon routing holes and the electrode hole are 0.25 mm and 0.17 mm respectively, primarily to reduce friction with the post-processed 3D-printed parts. Four of the nine tendons are used for assembly. They are spaced 90° apart, as seen in Fig. 2(b), and run through

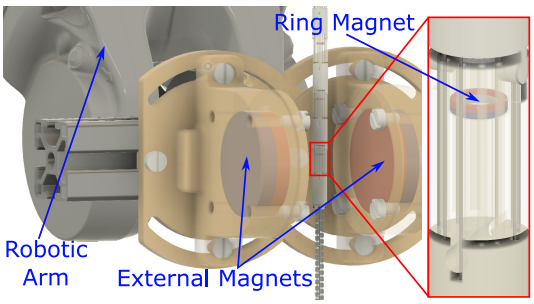

Fig. 3: Magnetic locking setup showing polarity of external and ring magnets

the hinges to constrain their movement to one axis. The remaining tendons are used to control the movement of the robot or to operate a latching mechanism, which grasps the SCS lead within its lumen. The links near the nitinol segment are deliberately made hollow to house a small axially-magnetised ring magnet. All the ring magnets within the body face the same direction (shown in Fig. 3) and will be used for locking the shape of the compound tube.

This design was preferred over a compound tube comprised of 3D-printed ball-joints, shown in Fig. 4(a), because of reduced axial compression upon tendon actuation. The compression in the ball-joint tube stemmed from its compromised integrity from having a hollow ball joint that allows the electrode to pass through as seen in Fig. 4(b). Axial compression leads to complications with the operation of the latching mechanism (discussed in following sections) and was the underlying reason for our use of the hinge design.

2) Nitinol Body: A nitinol tube with a length of 82 mm, an outer diameter (OD) of 4 mm, and an inner diameter (ID) of 3.4 mm, was machined using a Wire Electrical Discharge Machining unit (Additive Manufacturing Institute of Science and Technology, University of Louisville). A pattern of 1 mm rectangular notches, spaced 0.5 mm apart, were machined on either side of the nitinol tube in an alternating pattern to form bidirectional asymmetric joints that achieve 1-DoF bending [17]. The nitinol tube has two such 1-DoF bending joints as highlighted in Fig. 2(a-3), segment 2 (56.5 mm) and segment 3 (9.5 mm). Segment 2 primarily bends within the dorsal-ventral plane (of the patient's body upon insertion), while segment 3 is restricted to the lateral plane by the rotated slit patterns by 90° around the nitinol tube. Three tendons (drive tendons) of 0.2 mm diameter were anchored to the nitinol body using knots around 0.7 mm notches at the distal end of each segment. Actuation of the tendons results in bending. 2 mm thick tendon routing brackets were 3D-printed and attached to the nitinol body (using UV-glue) at every 12 mm interval in segment 2 and in the middle of segment 3. Each tendon routing bracket houses 6 holes: one in the center to facilitate the electrode, and the rest for tendon routing (spread around the circumference of the bracket). The drive tendons were placed parallel to their anchor points, while the tendons controlling the latching mechanism were offset from the lateral drive tendons by 27° as seen in Fig. 2(b). The clearance in these brackets were much smaller than the compound tube at 0.1 mm. An alternate pattern of notches with 0.1 mm slits spaced 0.7 mm apart (shown in Fig. 4(c)) was evaluated. This design demonstrated higher compliance;

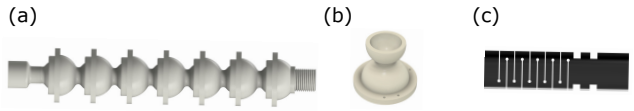

Fig. 4: (a) Alternative ball-joint tube design (b) Individual link of ball-joint tube (c) Alternative notched tube design

however, it was susceptible to axial compression and was phased out as a result.

3) Latching Mechanism: As it is illustrated in Fig. 2(c), the distal end of the nitinol segment houses a spring-loaded latching mechanism comprised of four parts: an actuating set of jaws, a jaw guide, a spring (spring constant = 1.8 N/mm), and a mounting bracket for the spring. The actuating jaws are a canister with a base on one side, to which tendons are attached, and four prongs with beveled edges on the opposing side. Each prong has a 0.202 mm notch extruded at the distal end contributing to increased compression and latching of the electrode. The jaw guide sits outside the nitinol tube and protrudes past the body by 0.9 mm in diameter. The upper chamber has a decreasing diameter based on an experimentally determined angle. The jaw guide was printed using a Formlabs Form 3 using clear resin for its increased strength and resistance to deformation.

The actuating set of jaws are pushed by the spring into the walls of the guide and are forced to clamp onto the electrode as the diameter of the guide decreases. The latching mechanism remains engaged as its ground state and the two tendons attached to the base of the jaws are pulled to disengage the mechanism. In doing so, the spring is compressed and the jaws are moved to a location within the guide with a higher diameter, thus freeing the electrode. Desirable function of the latching mechanism depends on minimal axial compression of the ExoNav body (since it interferes with the compression of the latching mechanism spring) as the latching mechanism tendons are pulled. Using this latching mechanism, the electrode is gripped tightly within the ExoNav while it is navigated to a target location. Upon reaching the target, the tendons actuating the latching mechanism are engaged, deploying the electrode at the target, while the ExoNav can be retrieved to deploy more electrodes.

B. Back-end Design

In the back-end section, the mechanism for operating the robot involves the use of four DC motors (ϕ8 mm, Maxon Metal Brushes, 0.5 Watt), which are affixed to a bracket at the rear of the back-end and powered by a 12V DC power supply. Nominal speed and torque are 3490 rpm and 0.623 mNm respectively. The motors used for actuating drive tendons use a 1:64 planetary gearbox, while the motor operating the latching mechanism is paired with a 1:16 planetary gearbox. Each motor is connected to a lead screw; by rotating this screw, a nut undergoes linear motion, facilitating the actuation of a 3D printed part, to which a 0.2 mm nitinol tendon is attached. Along each lead screw, two 3 mm rods and linear ball bearings allow for precise linear motion. In Fig. 2(a-4) we provide an illustration of this design. The device's outer diameter, set at 48 mm, facilitates ease of handheld operation.

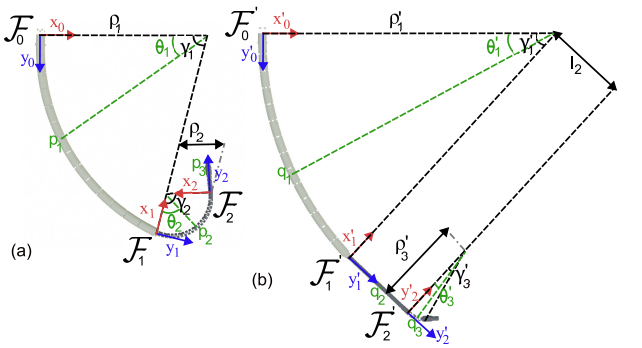

Fig. 5: Schematics of the robot bending in (a) dorsal and (b) lateral directions with the coordinate systems and curvature parameters shown.

III. Kinematic Model

In this section, a geometric kinematic model is proposed to predict the shape of the robot. This kinematic model is built upon multiple assumptions based on the constant curvature assumption (proven to work well for modeling bidirectional asymmetric notched tubes [17]) and the utilized design and manufacturing process of the robot. The bending curvatures for each part of the robot (namely proximal and distal tubes) are constant, the axial compression of the tubes is insignificant, bending forces and moments generated by the corresponding tendons for lateral bending is independent of the ones for dorsal bending, and the proximal compound tube bends in the same direction as the distal nitinol tube.

The robot is considered to have three different bending segments: the proximal compound tube, the distal nitinol tube segment responsible for dorsal bending (in the sagittal plane of the patient's body), and the distal nitinol tube segment responsible for lateral bending (in the coronal plane of the patient's body), and these different segments are denoted by subscripts 1, 2, and 3 respectively. Having these considerations in mind, the model is developed for two cases below:

A. Case 1: Dorsal Bending

In this case, segment 2 bends in its specific direction, and based on the fourth assumption previously mentioned, the proximal compound tube (segment 1) bends in the same direction as segment 2. On the other hand, the tendons to bend the robot to lateral directions are not actuated and consequently segment 3 remains straight throughout this case's scenario. Each bending segment has its specific radius of curvature (ρ_1 and ρ_2) and degree of curvature (γ_1 and γ_2) as shown in Fig. 5(a). Geometrically, these bending curvature parameters are constrained as $\rho_1\gamma_1 = l_1$ and $\rho_2\gamma_2 = l_2$, where l_1 and l_2 are the fixed segment lengths for the proximal segment and the lateral bending segment, respectively. Furthermore, a proportional relation between the two radii of curvature can be defined as:

$$\rho_2 = \mu\rho_1 \tag{1}$$

Here, $0 \leq \mu \leq 1$ is defined as the magnetic locking factor for dorsal bending. This factor equals 1 in the absence of magnetic locking effect. To relate the length of tendon stroke (ΔL) to the curvature parameters introduced above, one can write the following geometrical equation:

$$r_{t-1}\gamma_1 + r_{t-2}\gamma_2 = \Delta L \tag{2}$$

where r_{t-1} and r_{t-2} are the radii of the tendon routing channels, or in other words, the distance of tendons from the center-line of the robot in the subscripted segments respectively (these dimensional parameters are measured as $r_{t-1} = 2.75$ mm and $r_{t-2} = r_{t-2} = 1.263$ mm). By replacing the degrees of curvature in Eq. (2) by their alternative expressions, the following relation between ρ_1 and ΔL (i.e. robot-independent kinematic model) is obtained:

$$\rho_1 = \frac{\mu l_1 r_{t-1} + l_2 r_{t-2}}{\mu \Delta L} \tag{3}$$

Note that all the terms in Eq. (3) are known and fixed values, except for ρ_1 and ΔL. ρ_2 is also obtained simply by substituting the resulted ρ_1 into Eq. (1). Now that the robot-independent relations are obtained, the trajectory of an arbitrary point along the robot can be predicted in terms of the tendon stroke ΔL. However, to account for additional effects, a robot-dependent model is required. To develop this, geometry rules and relations will be used, and curvature parameters play an intermediate part between the tendon stroke ΔL and the position vectors p_i^0 (superscript 0 determining that p_i is expressed in the global fixed coordinate system $\mathcal{F}_0$). Based on the segment on which the arbitrary point p_i is defined, the equations used to obtain this position vector might change (due to different bending behaviors of different segments). Therefore, the arc-length of where the arbitrary point p_i is defined depends on which segment p_i is under consideration, and this will determine which equation has to be used. To do so, the subscript i will be 1,2, and 3, while defined on the segments 1, 2, and 3 respectively. To obtain unified mathematical equations that deal with both rotation and translation of the coordinate frames simultaneously, all the position vectors and transformation matrices that come in the following are presented in the special Euclidean group ($SE(3)$).

First, we explicitly define a transformation matrix in $SE(3)$:

$$A_j^k(\alpha) = \left(\begin{array}{c|c} R_j^k(\alpha) & a_j^k \\ \hline 0 & 1 \end{array}\right) \tag{4}$$

where the matrix $R_j^k(\alpha) \in \mathrm{SO}(3)$ is a rotation matrix that transforms the vectors defined in coordinate frame $\mathcal{F}_j$ suitably so that the resulted new vectors are expressed in coordinate frame $\mathcal{F}_k$. Furthermore, $a_j^k \in \mathbb{R}^3$ is the position vector (represented according to frame k axis directions) beginning from the origin of $\mathcal{F}_k$ and ending at the origin of $\mathcal{F}_j$.

Now, let's consider the case when p_i is defined on the proximal compound tube ($s \in [0, l_1]$ where s is the arc length from the base of the robot, where the origin of the global coordinate frame $\mathcal{F}_0$ is located, to the location where arbitrary point is positioned). In this case, the position vector p_1 is defined based on geometric relations for arcs with constant curvature:

$$p_1^0 = \begin{bmatrix} \rho_1(1 - C_{\theta_1}) & \rho_1 S_{\theta_1} & 0 & 1 \end{bmatrix}^T \tag{5}$$

Henceforth, the shorthand C and S will be used to indicate the cosine and sine functions respectively. In Eq. (5), the degree of curvature between the origin of $\mathcal{F}_0$ and the point p_1 is denoted by θ_1. Without loss of generality, θ_i is defined as the degree of curvature between the origin of $\mathcal{F}_{i-1}$ and the point p_i $(i = 1, 2, 3)$.

If the arbitrary point is defined on segment 2 ($s \in [l_1, l_1 + l_2]$), the arbitrary point p_2 can be expressed in the local coordinate system $\mathcal{F}_1$ as:

$$p_2^1 = \begin{bmatrix} \rho_2(1 - C_{\theta_2}) & \rho_2 S_{\theta_2} & 0 & |1| \end{bmatrix}^T \tag{6}$$

thus to express p_2^1 in the global coordinate frame $\mathcal{F}_0$, the following equation is used:

$$p_2^0 = A_1^0(-\gamma_1)p_2^1 \tag{7}$$

Ultimately, the case when the point is located on segment 3 ($s \in [l_1 + l_2, l_1 + l_2 + l_3]$) is analyzed. Since the segment 3 does not bend in the case of dorsal bending, the expression for the position vector in the local coordinate system $\mathcal{F}_2$ is different from the one for p_2^1 in Eq. (6):

$$p_3^2 = \begin{bmatrix} 0 & s - (l_1 + l_2) & 0 & |1| \end{bmatrix}^T \tag{8}$$

which is expressed in coordinate system $\mathcal{F}_0$, using the following equation:

$$p_3^0 = A_1^0(-\gamma_1)A_2^1(-\gamma_2)p_3^2 \tag{9}$$

B. Case 2: Lateral Bending

In this case, the same approach as Case 1 is taken. Similar to the above case, segment 1 bends in the direction of the total bending. Although, the difference appears in the other segments, where segment 2 stays straight while segment 3 bends to one of the lateral directions as illustrated in Fig. 5(b). Therefore, the proportional relation of the radii of curvatures for segments 1 and 3 is defines as:

$$\rho_3' = \mu' \rho_1' \tag{10}$$

Similar to the magnetic locking factor introduced in Eq. (1), μ' can take values between 0 and 1, with 1 used when the magnetic locking is not activated.

The global coordinate system $\mathcal{F}_0$ is rotated about the y_0 axis and all the other coordinate frames are rotated suitably, so that the z_i axes $(i = 1, 2)$ is orthogonal to the bending plane. The rotated coordinate systems are denoted as $\mathcal{F}_i'$ (i=0,1,2). The following translation matrix is utilized to rotate all the obtained position vectors back to the original coordinates orientation introduced in sub-section III-A:

$$A_{\mathcal{F}'}^{\mathcal{F}} = \left(\begin{array}{c|c} R_y(\beta) & 0 \\ \hline 0 & 1 \end{array}\right) \tag{11}$$

where β can be either $90°$ (if steering to the right direction while dorsal bending considered as steering upward) or $-90°$ (if steering to the left, following the same assumption mentioned earlier).

Furthermore, for segment 3 lateral bending, position vectors pointing to the arbitrary point along the robot will be denoted by q_i^j, with i and j used for the same purpose as in sub-section III-A. Note that the prime postscripts are used to determine whether the coordinate frame is a rotated one, or the curvature parameter is defined for lateral bending scenarios and the physical interpretation of these items are the same as their corresponding items in subsection III-A.

Starting with position vector corresponding to an arbitrary location on segment 1 ($s \in [0, l_1]$), a similar equation to Eq. (5) with suitable changes can be utilized:

$$q_1^0 = \begin{bmatrix} \rho_1'(1 - C_{\theta_1'}) & \rho_1' S_{\theta_1'} & 0 & |1| \end{bmatrix}^T \tag{12}$$

Secondly, while the arbitrary point is located on segment 2 ($s \in [l_1, l_1 + l_2]$) which will not bend in this case of the kinematic modeling, then the local position vector according to $\mathcal{F}_1'$ will be:

$$q_2^1 = \begin{bmatrix} 0 & s - l_1 & 0 & |1| \end{bmatrix}^T \tag{13}$$

and to express this in the rotated global fixed coordinate system $\mathcal{F}_0'$, the following equation is used:

$$q_2^0 = A_1^0(-\gamma_1')q_2^1 \tag{14}$$

Finally, to have the trajectory of the point located on segment 3 ($s \in [l_1 + l_2, l_1 + l_2 + l_3]$), the local position of the arbitrary point is written as:

$$q_3^2 = \begin{bmatrix} \rho_3'(1 - C_{\theta_3'}) & \rho_3' S_{\theta_3'} & 0 & |1| \end{bmatrix}^T \tag{15}$$

where θ_3' is the local degree of curvature that determines the location of the point q_3 on segment 3. Similar to the approach taken for obtaining Eq. (9), one can get to the q_3 expressed in $\mathcal{F}_0'$ using:

$$q_3^0 = A_1^0(-\gamma_1')A_2^1(0)q_3^2 \tag{16}$$

IV. Experiments and Results

A. Latching Mechanism Experiments (Isolated)

To test the efficacy of the latching mechanism, multiple experiments were conducted independent of the nitinol body while changing two variables: the angle of the jaw guide, and initial spring compression ,as seen in Fig. 6(a). Three different angles (δ = 3.3°, 5.5°, and 7.7°) and two levels of initial compression (0 mm and 1 mm compression) were examined throughout these experiments. The jaw guide angle of δ = 7.7° was the absolute maximum angle that could be accommodated before obstructing the electrode, while δ = 3.3° was the smallest angle to maintain tolerances between the latching mechanism and the guide while achieving latching. A total of 1 mm of compression was chosen to keep space for the latching mechanism to operate, travel, and unlatch within the jaw guide. A series of four different tests were conducted to examine how the angle of the jaw guide and initial compression of the spring affected the latching mechanism's functionality.

Test 1 examined the overall strength of the latching mechanism and used the following experimental setup: a load cell (MDB-5 5lb capacity, Transducer Techniques) was attached to a linear actuating platform, while the latching mechanism was clamped onto a stationary platform, as illustrated in Fig. 6(a). The electrode was pulled by the load cell equipped actuating platform while the latching mechanism was engaged to observe the maximum force exerted before failure. In this test, the jaw guide with δ = 3.3°, exerted the least amount of force (0.52 N). This jaw guide was outperformed by δ = 5.5° and δ = 7.7°, which exerted 4.12 N and 6.28 N respectively, as seen in Table II and Fig. 6(b-2

TABLE I: Force Values of Jaw Guides using 0 mm initial compression

	Stabilized values (N)			Peak values (N)	
δ	Engaged	Unlatching Force	Disengaged	Engaged	Disengaged
3.3°	0.04	–	0.008	0.079	0.099
5.5°	0.36	0.57	0.072	0.42	0.42
7.7°	0.80	0.84	0.004	0.93	0.93

TABLE II: Force Values of Jaw Guides using 1 mm initial compression

	Stabilized values (N)					Peak values (N)		
δ	Engaged	Engaged (no ST)	Unlatching Force	Unlatching Force (no ST)	Disengaged	Engaged	Engaged (no ST)	Disengaged
3.3°	0.52	–	2.20	–	0.19	1.24	–	0.6
5.5°	4.12	2.66	3.86	6.13	0.26	6.54	4.54	0.5
7.7°	6.28	1.86	3.73	5.23	0.22	10.13	4.10	0.53

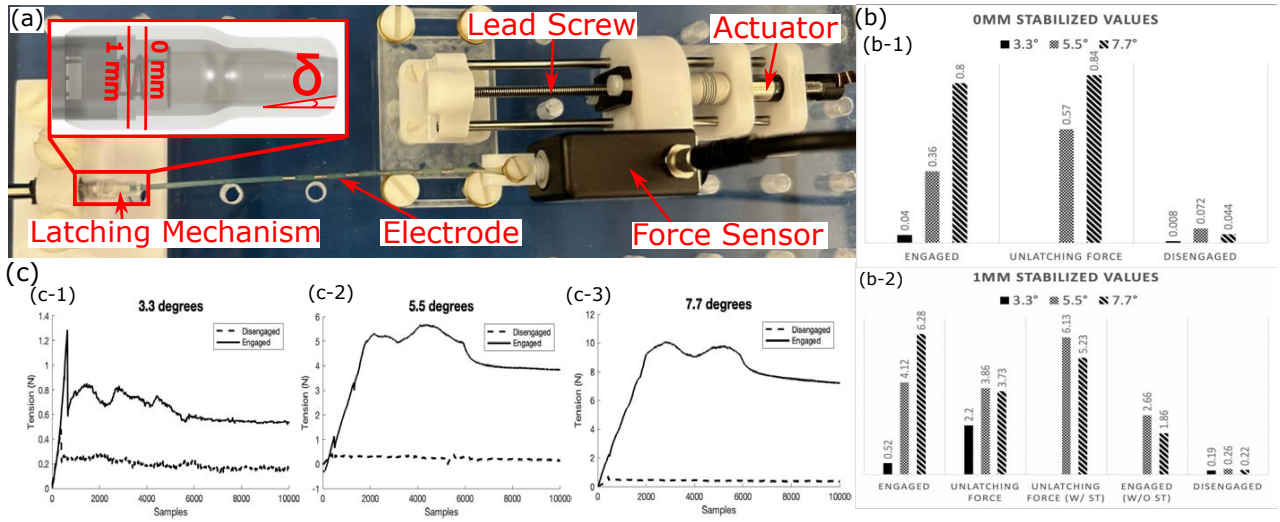

Fig. 6: (a) Isolated latching mechanism setup, representation of jaw guide angles, and initial compression (b) graphical representation of latching mechanism data (c) Force plots of each jaw guide (3.3°, 5.5°, 7.7° respectively) when latching mechanism is engaged vs. disengaged.

(Engaged)). Jaw guides with these angles also experienced a self-tightening (ST) effect – as the electrode was pulled, the jaws were dragged further into the jaw guide leading to increased clamping. When the initial compression of the spring was decreased from 1 mm to 0 mm, all the guides experienced a significant reduction in clamping ability. The δ = 3.3° jaw guide showed little to no signs of clamping (0.04 N), while the δ = 5.5° jaw guide applied 0.36 N, and the δ = 7.7° jaw guide applied 0.80 N, as seen in Table: I and Fig. 6(b-1) (Engaged). Along with the decrease in force, no signs of ST within the jaw guides was observed.

Test 2 quantified the unlatching force and validated the presence of ST. The experimental setup used was the same as test 1, rather, the load cell equipped platform pulled the latching mechanism tendons instead of the electrode. First, a baseline was established by recording the unlatching force without pulling the electrode. Next, the electrode was pulled until the latching mechanism failed and then the unlatching force was re-recorded. The unlatching force of δ = 3.3° jaw guide with ST was 2.20 N, however, in the absence of ST, latching was compromised and an unlatching value could not be derived. The unlatching force without ST for jaw guides with δ = 5.5° and δ = 7.7° was reduced by 2.27 N and 1.5 N respectively, as illustrated in Table: II and Fig. 6(b-2) (Unlatching Force)). The jaw guides with reduced initial compression experienced reduced unlatching forces and did not show any signs of ST. The δ = 3.3° jaw guide did not show any evidence of latching and did not have a specific force at which it unlatched. However, the δ = 5.5° jaw guide required 0.57 N to unlatch, and the δ = 7.7° jaw guide required 0.84 N to unlatch, as seen in Table: I and Fig. 6(b-1) (Unlatching Force).

In test 3, the strength of the latching mechanism without ST was examined. This test employed the same setup and procedure as test 1, however, the tendons attached to the internal jaws were anchored to the platform to prevent their further movement into the jaw guide and thus eliminating ST. Without ST, the δ = 5.5° and δ = 7.7° jaw guides exerted a peak force of 4.54 N and 4.10 N, and stabilized at 2.66 N and 1.86 N, as seen in Table: II and Fig. 6 (Engaged w/o ST). The lower compression jaw guides and the high compression δ = 3.3° jaw guide were not tested since there was no evidence of ST.

Finally, the design of the ExoNav requires minimal friction for easy passage of the electrode throughout the body. The last test examined the amount of friction applied on the electrode while the latching mechanism was disengaged. The setup used was the same as the first test, however, the tendons

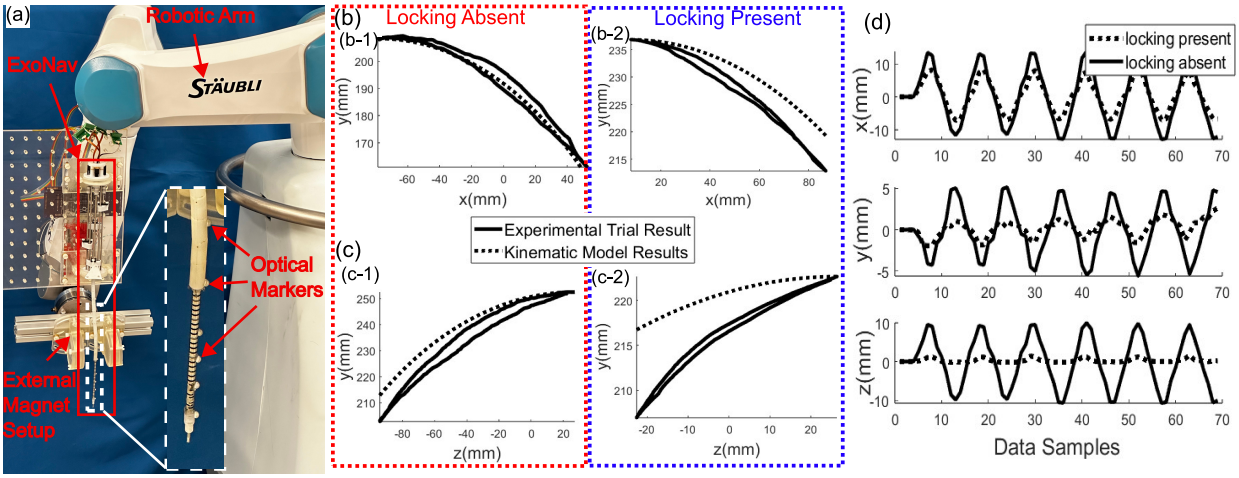

Fig. 7: (a) The experimental setup used for conducting free space experimental trials. (b) Comparing experimental data with kinematic model predictions for (b-1) dorsal bending when magnetic locking is absent and (b-2) when it is present. (c) Comparing experimental data with kinematic model predictions for (c-1) dorsal bending when magnetic locking is absent and (c-2) when it is present. (d) comparing robot active oscillation in absence and presence of magnetic locking.

controlling the actuating jaws were pulled and anchored in order to disengage the latching mechanism. Among the 1mm initial compression jaw guides, the $\delta = 3.3°$ jaw guide had the least amount of friction, at 0.19 N, while the $\delta = 5.5°$ and $\delta = 7.7°$ jaw guides exerted 0.26 N, and 0.22 N respectively, as seen in Table II and Fig. 6(b-2) (Disengaged). The decreased compression jaw guides had consistently lower values of friction with all three jaw guides below 0.072 N, as seen in Table I and Fig. 6(b-1) (Disengaged).

B. Latching Mechanism (on Robot)

The latching mechanism was installed on the robot with the $\delta = 7.7°$ jaw guide and put through two tests to characterize interactions between the latching mechanism and the nitinol segment. First, the robot was clamped down to the test bench where the nitinol tube and the compound tube connect and the electrode was pulled to failure. Then, the robot was clamped at the tip behind the latching mechanism. The first scenario under-performed in comparison to the isolated tests, achieving a maximum force of 8.32 N, while the second scenario achieved a force of 9.74 N. Finally, the friction between the electrode and the overall body was tested by disengaging the latching mechanism and measuring the force while pulling the electode. There was approximately 0.218 N of force between the electrode and the robot.

C. Free Space Trial

The kinematic model proposed in section III was validated in this section by conducting multiple experimental trials in free space under different circumstances. The experimental setup is illustrated in Fig 7(a). Several optical markers were strategically placed along the ExoNav robot body and were tracked by four Vero v2.2 motion tracking cameras. Additionally, three sets of markers were positioned at the in a fixed location to establish a global frame for the entire robot. The robot was installed on a stand in a vertical orientation to mitigate the influence of gravity on the initial shape of the robot.

These experiments were divided into four different parts which include bending the robot in the dorsal direction with and without magnetic locking effect, and correspondingly, bending the robot laterally either to the left or to the right position with and without magnetic locking effect. The data gathered from these experiments were processed and compared with the kinematic model predictions in Fig. 7(b)-(c). Using the gathered data, the magnetic locking factor was tuned and put equal to 0.6 (the same value was found for both factors μ and μ'). Additionally, in a data-driven manner, tendon extension and dead-zone effects were characterized and added to the kinematic model. The kinematic model worked precisely in predicting the trajectory of the robot's end-effector when the magnetic locking effect was not present, as depicted in Fig. 7 (b-1) and (c-1). Although, while magnetic locking was effective, the kinematic model failed to predict the trajectory of the tip of the robot accurately, as seen in Fig. 7 (b-2) and (c-2)), which was probably due to nonlinear behavior of the magnets and uncertainty in selection of the magnetic locking factor value.

D. Active Oscillation and Magnetic Locking Effect

To illustrate the magnetic locking effect in compensating the movements of the proximal part of the ExoNav robot, a set of active oscillation trials were carried out. In these experimental trials the robot was forced to swing laterally by actuating the tendons in absence and presence of the magnetic locking effect. The position of the far-end part of the compound tube was tracked and compared throughout these trials. As seen in Fig. 7(d), the magnetic locking mechanism successfully reduced the movements in X and Y directions. Additionally, when the magnetic locking was effective, the undesirable movements along the z-axis almost decreased to zero. These undesirable movements in the z-axis were most probably due to slight imperfections in alignment of drive tendons routing channels. Note that the ideal locking mechanism keeps the far-end of the proximal compound tube in place, but due to the non-contact approach of the utilized locking mechanism and limitations in the applicable magnetic field, some motions are still visible (especially in the X direction). However, if these motions are small enough

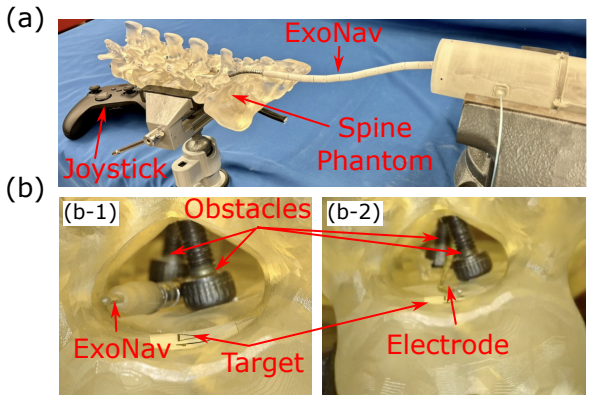

Fig. 8: (a) Trial setup, (b) ExoNav and electrode in the Spine Phantom during trials.

to guarantee a collision-free procedure, this magnetic locking effect can be acquired.

E. Experiment in The Spinal Cord phantom

A neurosurgeon, who is also a co-author of this paper, conducted timed trials to navigate the ExoNav and the standard SCS electrode around obstacles to a target in a phantom spinal cord (experimental setting with the ExoNav is shown in Fig. 8). In trials with two obstacles, manual and robot trials took similar time (average time of 63.99 s and 61.75 s respectively), but manual trials had higher inconsistency with a standard deviation of 22.72 s (compared to 0.47 s) as the slightest differences in positioning caused greater difficulty for navigation. With three obstacles, manual trials were faster (average time of 24.18 s compared to 45.15 s) but as the surgeon became accustomed with navigating the obstacles, the time required for both methods of navigation improved (average manual time of 5.36 s and an average time of 16.23 s with the ExoNav). Finally, after training on this trajectory, a new trajectory was presented to the surgeon. In these trials the average time gap between manual (Average time of 17.7 s) and ExoNav (Average time of 24.72 s) was lower, although the manual approach was still faster.

This extended duration of trials with the ExoNav can be attributed to the high gearing of the drive motors (1:64) which limited the reachable linear velocity of the tendon pulling assembly (about 0.5 mm/s). Additionally, the smaller diameter of the electrode (1.6 mm compared to 4.2 mm) facilitated easier navigation through the obstacles. However, this trial was conducted simply as a proof-of-concept of the efficacy of our device in steering SCS electrodes. A rigorous expert surgeon trial with surgeon participants will be the subject of our future work.

V. Conclusions and Future Work

In this paper we developed both a novel steering mechanism and a latching mechanism, to steer SCS electrodes within epidural cavities. The latching mechanism has a universal design that could be used in other cases where grasping is required via a catheter. Depending on the parameters, this mechanism can provide up to 10.13 N of force and has the potential to be an effective design. Furthermore, magnetic non-contact locking proved to be an effective stabilization technique in the ExoNav but requires further development and optimization for practical usage. The current prototype does have its limitations: its large size and limited dexterity make it difficult to navigate in epidural space. Our future work will address additional time-trials with neurosurgeons along with modifying the ExoNav design to grasp SCS electrodes from the side and by implementing high compliance follow-the-leader motion strategies in the distal tip.

References

[1] J. Dahlhamer, J. Lucas, C. Zelaya, R. Nahin, S. Mackey, L. DeBar, R. Kerns, M. Von Korff, L. Porter, and C. Helmick, "Prevalence of chronic pain and high-impact chronic pain among adults—united states, 2016," *Morbidity and Mortality Weekly Report*, vol. 67, no. 36, p. 1001, 2018.

[2] H. Knotkova, C. Hamani, E. Sivanesan, M. F. E. Le Beuffe, J. Y. Moon, S. P. Cohen, and M. A. Huntoon, "Neuromodulation for chronic pain," *The Lancet*, vol. 397, no. 10289, pp. 2111–2124, 2021.

[3] A. Rupp, V. T. Francio, J. M. Hagedorn, T. Deer, and D. Sayed, "The impact of spinal cord stimulation on opioid utilization in failed back surgery syndrome and spinal surgery naïve patients," *Interventional Pain Medicine*, vol. 1, no. 4, p. 100148, 2022.

[4] J. D. MacDonald and K. J. Fisher, "Technique for steering spinal cord stimulator electrode," *Operative Neurosurgery*, vol. 69, pp. ons83–ons87, 2011.

[5] H. Torlakcik, C. Sarica, P. Bayer, K. Yamamoto, C. Iorio-Morin, M. Hodaie, S. K. Kalia, J. S. Neimat, J. Hernesniemi, A. Bhatia *et al.*, "Magnetically guided catheters, micro-and nanorobots for spinal cord stimulation," *Frontiers in Neurorobotics*, vol. 15, p. 749024, 2021.

[6] Y. Chitalia, X. Wang, and J. P. Desai, "Design, modeling and control of a 2-dof robotic guidewire," in *2018 IEEE International Conference on Robotics and Automation (ICRA)*. IEEE, 2018, pp. 32–37.

[7] S. Jeong, Y. Chitalia, and J. P. Desai, "Design, modeling, and control of a coaxially aligned steerable (coast) guidewire robot," *IEEE Robotics and Automation Letters*, vol. 5, no. 3, pp. 4947–4954, 2020.

[8] Y. Chitalia, A. Sarma, T. A. Brumfiel, N. J. Deaton, M. Sheft, and J. P. Desai, "Model-based design of the coast guidewire robot for large deflection," *IEEE Robotics and Automation Letters*, 2023.

[9] A. Sarma, T. A. Brumfiel, Y. Chitalia, and J. P. Desai, "Kinematic modeling and jacobian-based control of the coast guidewire robot," *IEEE Transactions on Medical Robotics and Bionics*, vol. 4, no. 4, pp. 967–975, 2022.

[10] A. Sarma, G. C. Collins, N. Nayar, Y. Chitalia, S. Jeong, B. D. Lindsey, and J. P. Desai, "Towards the development of an ultrasound-guided robotically steerable guidewire," in *2020 International Symposium on Medical Robotics (ISMR)*. IEEE, 2020, pp. 173–180.

[11] S. Fu, B. Chen, D. Li, J. Han, S. Xu, S. Wang, C. Huang, M. Qiu, S. Cheng, X. Wu *et al.*, "A magnetically controlled guidewire robot system with steering and propulsion capabilities for vascular interventional surgery," *Advanced Intelligent Systems*, p. 2300267, 2023.

[12] S. Zhang, M. Yin, Z. Lai, C. Huang, C. Wang, W. Shang, X. Wu, Y. Zhang, and T. Xu, "Design and characteristics of 3d magnetically steerable guidewire system for minimally invasive surgery," *IEEE Robotics and Automation Letters*, vol. 7, no. 2, pp. 4040–4046, 2022.

[13] Y. Haga, T. Mineta, and M. Esashi, "Active catheter, active guide wire and related sensor systems," in *Proceedings of the 5th Biannual World Automation Congress*, vol. 14. IEEE, 2002, pp. 291–296.

[14] X. Hu, A. Chen, Y. Luo, C. Zhang, and E. Zhang, "Steerable catheters for minimally invasive surgery: a review and future directions," *Computer Assisted Surgery*, vol. 23, no. 1, pp. 21–41, 2018.

[15] T. Ranzani, S. Russo, F. Schwab, C. J. Walsh, and R. J. Wood, "Deployable stabilization mechanisms for endoscopic procedures," in *2017 IEEE International Conference on Robotics and Automation (ICRA)*. IEEE, 2017, pp. 1125–1131.

[16] H. Wei, G. Zhang, S. Wang, P. Zhang, J. Su, and F. Du, "Coupling analysis of compound continuum robots for surgery: Another line of thought," *Sensors*, vol. 23, no. 14, p. 6407, 2023.

[17] Y. Chitalia, S. Jeong, N. Deaton, J. J. Chern, and J. P. Desai, "Design and kinematics analysis of a robotic pediatric neuroendoscope tool body," *IEEE/ASME Transactions on Mechatronics*, vol. 25, no. 2, pp. 985–995, 2020.